Composites: Part A 169 (2023) 107520

Contents lists available at ScienceDirect

Composites Part A

journal homepage: www.elsevier.com/locate/compositesa

Measurement and modelling of dynamic fluid saturation in carbon reinforcements

Helena Teixidó [a], Guillaume Broggi [a], Baris Caglar [b], Véronique Michaud [a,*]

[a] Laboratory for Processing of Advanced Composites (LPAC), Institute of Materials (IMX), Ecole Polytechnique Fédérale de Lausanne (EPFL), Station 12, 1015 Lausanne, Switzerland
[b] Aerospace Structures and Materials Department, Faculty of Aerospace Engineering, Delft University of Technology, Kluyverweg 1, Delft 2629HS, Netherlands

ARTICLE INFO

Keywords:
A. Carbon fibers
B. Wettability
C. Process Modeling
E. Resin Flow

ABSTRACT

We propose a methodology to monitor the progressive saturation of a non-translucent unidirectional carbon fabric stack through its thickness by means of X-ray radiography and extract the dynamic saturation curves using image analysis. Four constant flow rate injections with increasing flow speed were carried out. These were simulated by a numerical two-phase flow model for both capillary and viscous leading flow conditions. The hydraulic functions describing pressure and relative permeability versus saturation were determined by fitting the saturation curves using a heuristic optimization routine. As the fluid velocity increases and the flow regime at the flow front shifts from capillary to hydrodynamically driven, the resulting capillary pressure curves for a given saturation level are shifted to higher values, from negative to positive. These as well as the capillary pressure calculated from the pressure drop within the unsaturated region of the fabric correlate well with a corresponding change in the averaged dynamic contact angle.

1. Introduction

Liquid Composite Molding (LCM) techniques belong to infiltration processes whereby a resin is forced to ingress into a fibrous reinforcement placed inside a mold by applying a pressure differential. In order to obtain final composite parts with a minimal flaws content, an adequate control of the filling step is crucial to ensure that the highest fraction of the initial air is replaced by the infiltrating resin. Owing to the dual scale nature of engineering textiles, with micro- and *meso*-pores located respectively inside and in between the bundles, a dual scale flow is usually observed thus triggering a void entrapment mechanism. At the flow front, a constant competition between viscous and capillary forces takes place; depending on the infiltration speed, the pore size distribution and the wetting properties of the fluid, one of the two dominates the main flow. As the flow is pressure driven, dynamic wetting properties of the viscous resin on the reinforcement strongly depend on the fluid velocity for a given reinforcement-matrix material system [1,2]. Hence, resulting capillary forces determine whether the fabric can be spontaneously infiltrated, and thus flow within the tows will lead when the fluid phase wets the fibers, or whether the fabric is not spontaneously infiltrated, and pressure driven flow will lead between the tows, if the fluid phase is non-wetting. The filling pattern and in consequence the potential number of entrapped voids (which depends on fluid pattern as well as on textile geometry, in addition to the quantity of volatiles in the resin and/or initially entrapped air) will be determined by the extent of viscous versus capillary flows. The dimensionless capillary number is used to define the transition between these flow regimes:

$$Ca = \frac{U\eta}{\gamma} \tag{1}$$

where U, η, and γ are the fluid superficial velocity, viscosity and surface tension (in air) respectively. Researchers tend to agree with the existence of an optimal capillary number Ca_{opt}, for which capillary and viscous forces compensate each other resulting in minimal void content [3]. Since Ca_{opt} is also influenced by the textile architecture and the fiber volume fraction in addition to the fiber-fluid interface properties, it is specific for a given resin/reinforcement system and its value is generally measured experimentally [4].

Flow through porous media is governed by the interplay of several physical phenomena taking place at different scales, from the scale of the fiber/matrix interface to that of a tow, of an assembly of tows forming a textile, up to the full part, thus triggering a very complex process. Several approaches have been adopted to model the transport of fluid flow at the macro-scale as reported in Refs. [4,5]. For simplicity,

* Corresponding author.
E-mail address: veronique.michaud@epfl.ch (V. Michaud).

https://doi.org/10.1016/j.compositesa.2023.107520
Received 22 November 2022; Received in revised form 28 February 2023; Accepted 4 March 2023
Available online 9 March 2023

Nomenclature

α	Fluid phase
β	Van Genuchten law parameter [m^{-1}]
γ	Liquid surface tension [N/m]
ΔP	Pressure difference between the inlet and the outlet [Pa]
ΔP_γ	Capillary pressure drop [Pa]
ΔP_{sat}	Average ΔP in the saturated length [Pa]
η_α	Phase viscosity [Pa•s]
θ	Dynamic contact angle [°]
θ_0	Static contact angle [°]
θ_α	Phase volume content [-]
ρ_α	Phase density [kg/m^3]
τ	Capillarity or dynamic storage coefficient [Pa•s]
ϕ	Porosity of the porous media [-]
A	Preform cross section [m^2]
A_w	Fabric areal weight [g/m^2]
B	Arrhenius law fitting parameter [Pa•s]
C_α	Capacity of phase α [1/Pa]
Ca	Capillary number [-]
c_T	Tanner's law coefficient [-]
D	Error difference [%]
E	Objective function [-]
E_a	Arrhenius law fitting parameter [kJ•mol^{-1}]
g	Gravitational constant [m^2/s]
H_p	Pressure head [m]
$k_{r,\alpha}$	Relative permeability of phase α [-]
K_{sat}	Saturated permeability [m^2]
L	Van Genuchten law parameter [-]
L_f	Fabric length [m]
M	=1-1/N
N	Van Genuchten law parameter [-]
nw	Non-wetting phase
p_c	Local macroscopic capillary pressure [Pa]
p_α	Pressure in the phase α [Pa]
P_e	Entry pressure [Pa]
Q_{out}	Outcoming flow rate [m^3/s]
R	Gas constant [J•K^{-1}•mol^{-1}]
r_f	Fiber radius [μm]
$\dot{S}$	Desaturation rate [-]
S_α	Effective saturation of phase α [-]
S_f	Liquid-fiber interface per unit of liquid volume [m^{-1}]
t	Time [s]
T	Temperature [K]
u_α	Phase velocity [m/s]
U	Superficial velocity [m/s]
V_f	Fiber volume fraction [-]
w	Wetting phase
z	Vertical spatial coordinate [m]

infiltration studies often assume a sharp and fully saturated flow front but multiphase flow approaches have also been considered, following methods developed in many engineering branches such as soil science, for homogenous porous media [6]. Metal-based matrix infiltration made use of these multiphase methods [7–10] but they are still seldom applied to polymeric resins [11–14]. A continuum mechanics framework is applied, and a representative volume element is defined in which a resin phase displaces an air phase contained a fibrous porous medium. In order to solve the mass and momentum conservation equations for each phase, the definition of constitutive relationships for pressure vs saturation at the macro-scale, known as drainage-imbibition curves, as well as the relative permeability vs saturation are needed. Drainage is used for flow of a non-wetting resin into a preform initially containing the wetting phase whereas imbibition term is for flow of a wetting phase into a preform containing the non-wetting phase. These constitutive relationships are generally identified by inverse methods from experimentally acquired data describing saturation versus pressure or time during flow, in well controlled conditions [15,16]. However, flow visualization in such well controlled experiments is still a difficult task and often reserved to optically translucent preforms such as glass whereas flow observation through non-translucent preforms (e.g. carbon) has been barely addressed. For example, the progressive saturation has been elucidated in the case of glass fabrics by optical [11,13,14], thermal [12] and dielectric techniques [17,18]. Nowadays, X-ray based techniques are gaining interest, and given their versatility for non-destructive analysis of static and dynamic phenomena, the field is evolving rapidly. In particular, a significant reduction of acquisition times has allowed to image flow progression with unprecedented resolution. For example, Castro et al. [19] recently used a synchrotron radiation computed laminography to image 3D in-situ dual scale flows with micron-scale resolution at an acquisition rate of 1.8 min per tomogram. This method allowed them to study local void distribution and thus the progressive saturation, though at a small scale and low velocity when compared to real composite impregnation scales.

In Ref. [20], we proposed to use an X-ray phase contrast imaging device [21] to assess the progressive saturation of several distinct fibrous preforms even with conventional resins at velocities similar to those used in LCM processes, with acquisition rates below 10 s per radiograph. In particular, this technique is sensitive to the ultra-small angle scattering and allows to enhance the contrast between materials with similar density but with enough microscale heterogeneities. Good results were obtained with pressure driven flows, in particular for carbon fiber fabrics, yet, for flow rates where tow impregnation preceded, the necessary contrast to elucidate clear flow patterns from the scattering images was not achieved. In addition, this early work demonstrated the principle to extract saturation curves versus time during flow experiments, however, did not address the modelling aspects and extraction of relevant constitutive functions.

In the present work, we expand the observation method by exploring the use of contrasting agents to enhance the fluid/fabric contrast in the absorption images, gaining further details in the impregnation of a unidirectional carbon preform, thus with a rather uniform bi-modal pore size distribution. The progressive saturation is thus analyzed for injection conditions covering various flow regimes and modelled with a two-phase flow model as developed in Ref. [11], further extended to account for both wetting and non-wetting scenarios. An optimization procedure is proposed to extract the relevant constituting parameters from the experimental drainage-imbibition curves. Finally, we propose to link the results of the two-phase flow model with the macroscopic capillary pressure drop approach, based on saturated flow assumptions, through the averaged dynamic contact angle dependency on the capillary number.

2. Theory

A representative elementary volume (REV) is defined with the phases in presence: air, resin and fibers. Even though the fabric has a bimodal pore size distribution, we assume here that the separation of scales in the textile considered is small enough that a dual porosity approach is not necessary, [22,23], which will be further verified. In addition, as already suggested in previous work (Ref. [11]), and as will be discussed later, considering the rather high viscosity of the fluid as compared to water (as the fluid of consideration in soil science studies), we consider that flow takes place far from equilibrium conditions, and so that the

capillary pressure acting at the fluid/air interface depends on the flow rate conditions. Thus, the resin phase will be considered either wetting or non-wetting depending on the *Ca* value, and the air phase takes the opposite wetting properties. The two phases are thus defined as either wetting or non-wetting and their respective contents are θ_w and θ_{nw}. The available pore space, which is the porosity of the porous media ϕ ($\phi = 1 - V_f$, with V_f the fiber volume fraction, considered constant in what follows), is completely occupied by both phases:

$$\theta_w + \theta_{nw} = \phi \tag{2}$$

Before impregnation, no resin phase is contained in the porous preform, thus, no residual liquid content is considered and the degree of effective saturation S for each phase is directly defined as the ratio of the phase volume to the total free space as:

$$S_\alpha = \frac{\theta_\alpha}{\phi} \tag{3}$$

where α refers either to wetting (w) or non-wetting (nw) phase present in the preform. S varies between 0 and 1, 0 corresponding to a preform with no α phase, and 1 to a preform fully saturated with α phase. Consequently, their effective saturations are combined:

$$S_w + S_{nw} = 1 \tag{4}$$

Moreover, the two phases are coupled through their pressures with the macroscopic capillary pressure description p_c with the following relation:

$$p_c(S_\alpha) = p_{nw} - p_w \tag{5}$$

In LCM, the air pressure is generally atmospheric, and for simplicity it is set to zero as a baseline. The specific capacity C_α of each phase is defined as:

$$C_\alpha = \theta_\alpha \frac{\partial S_\alpha}{\partial p_c} \tag{6}$$

Note that the specific capacity is the same for the two phases but with opposite sign and are thus related as: $C_w = -C_{nw}$. Resin infiltration is modelled with a continuum mechanics approach [24]. It is commonly assumed that the resin is an incompressible Newtonian fluid (as well as the air) and that infiltration takes place without heat exchange (for non-isothermal cases, an equation for thermal transport can also be added). Mass conservation equation for each phase is written as follows:

$$\frac{\partial \theta_\alpha}{\partial t} + \nabla \bullet (\theta_\alpha u_\alpha) = \frac{\partial (\phi S_\alpha)}{\partial t} + \nabla \bullet (\phi S_\alpha u_\alpha) = 0 \tag{7}$$

where u_α is the average local fluid velocity. Equation (7) neglects gravitational or other momentum transfer between bodies and is only valid for a Reynolds number less than one, defined in relation to the average fluid velocity and the pore diameter. The mass balance equation for the solid phase in a rigid preform is null. Darcy's law is applied to write the momentum equation [25]:

$$\phi S_\alpha u_\alpha = -\frac{K_{sat} k_{r,\alpha}}{\eta_\alpha} \nabla p_\alpha \tag{8}$$

where K_{sat} is the preform saturated permeability tensor, $k_{r,\alpha}$ the relative permeability scalar (a function of S_α) which varies between 0 and 1 representing the ease of one phase to flow in the presence of another immiscible phase, η_α is the phase viscosity, considered to be constant through the impregnation, and p_α the pressure in the phase α. $\phi S_\alpha \vec{u}_\alpha$ from equation (8) is also defined as the superficial (or filtration) velocity U. Since the air pressure is assumed to remain close to zero, the governing equation for the fluid phase is reduced to Richards' equation as [26]:

$$C_\alpha \frac{\partial p_\alpha}{\partial t} + \nabla \bullet \left[-\frac{K_{sat} k_{r,\alpha}}{\eta_\alpha} \nabla p_\alpha \right] = 0 \tag{9}$$

Finally, to complete the equations describing the non-linear problem, initial and boundary conditions are defined as well as the retention and permeability relationships, $S_\alpha(p_c)$ and $k_{r,\alpha}(S_\alpha)$ respectively. Those hydraulic functions are generally not known and need to be identified experimentally. They can be described by semi-empirical expressions such as the ones proposed by Brooks and Corey [15] or by van Genuchten and Mualem [16,27,28] among others [5,29]. In the present work, van Genuchten and Mualem descriptions of retention and conductivity functions, S_α and $k_{r,\alpha}$ respectively, have been chosen for simplicity from the numerical simulation point of view [11,30] and because of their wide use for the prediction of the hydraulic functions:

$$S_w = \begin{cases} \dfrac{1}{\left(1 + |\beta H_p|^N\right)^M}, H_p > 0 \\ 1, H_p \le 0 \end{cases} \tag{10}$$

$$S_{nw} = 1 - S_w \tag{11}$$

$$k_{r,w} = \begin{cases} S_w^L \left[1 - \left(1 - S_w^{1/M}\right)^M\right]^2, H_p > 0 \\ 1, H_p \le 0 \end{cases} \tag{12}$$

$$k_{r,nw} = \begin{cases} S_{nw}^L \left[1 - (1 - S_{nw})^{1/M}\right]^{2M}, H_p > 0 \\ 1, H_p \le 0 \end{cases} \tag{13}$$

with $H_p = p_c/(\rho_\alpha g)$ the pressure head and L, N, M and β the van Genuchten parameters, which all depend on *Ca*, with $M = 1 - 1/N$. In general, hydraulic properties and the relation of these parameters to the system physical properties are assumed to be of a static nature as they are measured at capillary equilibrium: β is inversely dependent to the "bubbling pressure" (representing a pressure deriving from capillary forces, specific for a fluid/solid pair and its value is close but not equal to the capillary pressure) [7] and N and M are related to the particle size distribution of the porous media. According to the original work of Mualem [28] the parameter L accounts for the tortuosity and connectivity of the porous media and is usually set to 0.5. However, its physical meaning has been questioned since it often takes a negative value and in consequence it is just considered as a free fitting parameter [11,31,32]. Thus, these parameters are essentially curve shape parameters with no direct physical meaning that are directly fitted from data sets [31]. In our pressure driven flow case, depending on the fluid kinetics, the resin may be either the wetting or non-wetting phase, and the respective descriptions for saturation and permeability will be adapted accordingly. Hence, it is expected that hydraulic functions are unique for a given injection condition, namely the imposed flow rate, and that all parameters are functions of *Ca*.

In the present macroscopic approach, all effects and processes that will influence the ratio between the two fluid phases (such as surface tension, wettability of the solid, porosity distribution) are lumped into $p_c - S - k_r$ relationships for a given value of *Ca*. Moreover, since p_c is determined here under different injection conditions (the desaturation rate $\dot{S} = \partial S/\partial t$ is thus not equal to 0), it is regarded as a dynamic capillary pressure. Consequently, the difference between non-wetting and wetting pressures is not only due to capillary effects active at equilibrium state with no flow, but also depends on the flow dynamics (such as the pressure gradient needed to overcome viscous forces) [33]. Even if saturation curves are generally determined in literature under static conditions (and thus only dependent on the system properties), researchers proved that they lead to a poor prediction of two-phase flow kinetics in real non-steady cases. In particular, dynamic effects manifest themselves as differences in hydraulic functions descriptions [34,35]. Thus a dynamic capillary pressure, $P_{c,d}(S, \dot{S})$ with a more general thermodynamic definition, is increasingly employed and is related to the static one $P_{c,e}(S)$ by introducing a dynamic term dependent on the

temporal rate of saturation change τ, such that $P_{c,d}(S,\dot{S}) = P_{c,e}(S) - \tau\dot{S}$. This term τ, also called the capillarity coefficient, is a measure of the fluid speed to reach an equilibrium state. Even though some studies showed a dependence between τ and S, the functional relationship is still unclear [36–38]. Experimentally, the dynamic capillary pressure is observed to be greater than the static one in drainage and lower in imbibition, and their difference is suggested to arise from the change of static to dynamic contact angles [35,39–43]. This arises from the fact that capillary pressure (in a saturated slug-flow assumption) is related to the contact angle θ by the following expression: $\Delta P_\gamma = -S_f\gamma\cos(\theta)$, where S_f is the total surface of matrix-fiber interfaces per unit volume of the pore space [4,5]. The link between dynamic contact angle (which in this case corresponds to an averaged contact angles, as it is averaged over the whole REV) and capillary pressure obtained from the multi-phase flow approach is however not often directly made in the literature, in part because fluids used in soil science have a much lower viscosity than organic resins, hence less marked dependency of the contact angle on flow velocity.

3. Materials and methods

3.1. Materials

The quasi-unidirectional carbon fabric from Suter Kunststoffe AG ($A_w = 270$ g/m^2) previously employed in Ref. [20] was chosen as fibrous reinforcement. Its architecture is shown in Fig. 1, the fabric is plain weave with thin E-glass threads in the weft direction to maintain carbon tows in place, but considered to be unidirectional since carbon fibers are predominant (carbon $A_w = 260$ g/m^2 and glass $A_w = 10$ g/m^2). According to the datasheet, warp tows are made of sized carbon fibers Tenax HTA 3151 from Teijin with density 1.77 g/cm^3 and a diameter of 7 μm. The fabric is highly packed and the space between carbon tows has been measured to be less than 60 μm. The average width of the carbon tows was measured to be around 1.48 mm and the spacing between glass tows around 3.30 mm. As a result, this fabric is uniformly bi-modal and we do not expect this fabric to show extreme dual-scale effects as observed in other textiles where large flow channels are present [44]. We thus expect flow patterns to mostly relate to dynamic wetting effects.

The test fluid was an aqueous solution of poly(ethylene glycol) (PEG) (Mw = 35 kDa, Sigma Aldrich) mixed with a ZnI_2-based contrasting solution to increase the fluid-fabric contrast by X-ray absorption [45]. The resulting fluid formulation was 62.5 wt% of water, 11.0 wt% of PEG, 22.6 wt% of ZnI_2 (Mw = 319.19, Fluorochem) and 3.9 wt% of Kodak Photo-Flo 200. The density of the mixture was measured to be 1.276 g/ml. The viscosity of the system was measured in continuous shear mode in a concentric rheometer (AR2000ex, TA Instrument) by means of a Peltier Couette setup with a temperature ramp ranging from 18 °C to 30 °C at 0.1 °C/min at a constant shear-rate of 10 s^{-1} (Fig. 2). The temperature behavior was fitted with an Arrhenius law:

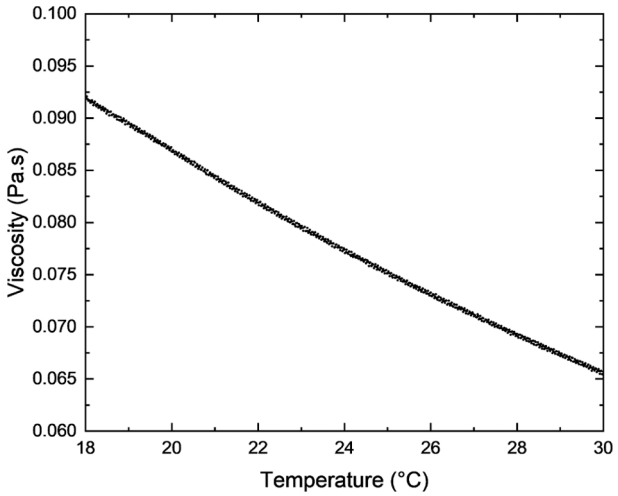

Fig. 2. Viscosity-temperature curve of the infiltrating fluid.

$$\eta(T) = Bexp\left[-\frac{E_a}{RT}\right] \tag{14}$$

where B and E_a are fitting parameters and equal to 1.715•10^{-5} Pa•s and −20.79 kJ•mol^{-1} respectively. The surface tension in air at ambient temperature (since the apparatus did not allow to perform temperature dependent measurements) was assessed by means of the pendant drop method with a Drop Shape Analyzer (DSA30, Krüss) and a value of 32.7 ± 0.2 mN/m was obtained, averaging four measurements. Since the fluid is water based, we estimated that the change in surface tension between experimental conditions varied by not more than 1 % [46].

For the permeability measurements, a water-based solution of poly (ethylene glycol) at 16.67 wt% previously characterized by Salvatori et al. [44] was employed.

3.2. Static contact angle assessment

The static contact angle θ_0 between the fluid and solid phases was measured following the drop-on-fiber method: a single carbon fiber was separated from a tow, taped straight into a metal frame and the liquid drops were sprayed onto the fibers. The droplets were imaged using a Keyence VHX-7000 microscope equipped with a zoom lens (100x to 1000x) and pictures were recorded with a resolution 1600 × 1200 pixels and a 4.18 pixel/μm ratio. Then, the length and height of the symmetrical droplets as well as the fiber diameter were measured and used for estimation of θ_0 following the geometrical analysis proposed by Carroll [47].

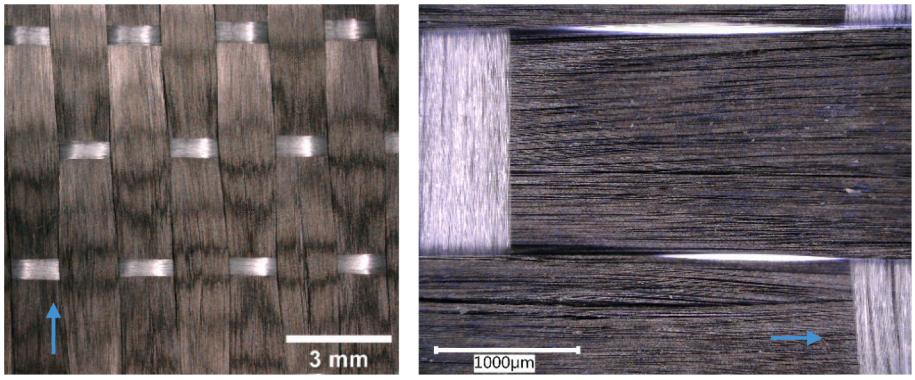

Fig. 1. Unidirectional carbon fiber reinforcement employed. The blue arrow indicates the warp direction (0°).

3.3. Flow experiments

Flow experiments were performed with the setup presented in Ref. [20]. Fabric layers were accurately hand-cut with a dimension of 4.95 ± 0.05 cm × 15 cm. Then, nine layers of fabric (direction 0°) were fitted into a mold made out of PMMA halves enclosed in between two metal frames fastened with screws with a 3 mm thick metal spacer to set the height cavity, leading to a fiber volume fraction, $V_f \approx 45$ %. A silicon joint was used to prevent race-tracking. In-plane injections were performed in the vertical position (from bottom to top, z-position) to align the flow with the orientation of X-ray source and detector. Close to the fluid inlet, a Keller Series 35XHTT sensor was placed to monitor the fluid pressure and temperature during the test. Constant flow rate experiments were carried out to maintain a constant capillary number during the impregnation. Four experiments were conducted at different flow rates to obtain a range of flow regimes spanning from capillary to viscous. The fluid velocity was adjusted by controlling the pump setting and was measured from the averaged front velocity from the saturation curves. The position for a $S = 0.5$ was extracted and plotted versus time and the average velocity corresponds to the slope of the linear fit (the time$t = 0$ s was set so the linear function was a proportional function). The resulting flow front velocity u and superficial velocity U, the average fluid temperature T with the respective viscosity η and capillary numbers Ca are listed in Table 1.

3.4. Permeability measurement

To solve equation (9), a proper measurement of the saturated permeability K_{sat} is first sought. Permeability experiments were performed with the same mold and setup configuration as the flow experiments, thus with an aspect ratio of 3 between length and width. At the outlet, a beaker and a scale were added to record the outcoming mass after full impregnation of the preform related to the outcoming flow rate Q_{out} with the fluid density. Before each experiment, the fabric stack was weighed to accurately estimate the fabric volume fraction. In an in-plane impregnation, K_{sat} can be easily calculated from the following relation derived from Darcy's law:

$$K_{sat} = \frac{Q_{out}\eta L_f}{A\Delta P_{sat}} \tag{15}$$

where L_f the fabric length, A the cross-section area of the fabric stack and ΔP_{sat} the average pressure difference across the saturated flow. Since in a constant flow rate, the pressure increases first linearly during the saturation of the preform and then becomes stable once the preform is saturated, the fluid was let to flow enough so the pressure was constant (varying ± 0.001 bar) to measure the saturated permeability. Three experiments per constant flow rate condition (same as tests #1 to #4) were carried out to elucidate if the K_{sat} was somehow dependent on the flow rate. The twelve permeability results as a function of the superficial velocity are shown in Fig. 3 and as no trend was observed, a mean value of K_{sat} was calculated resulting in an averaged value of $8.63\bullet10^{-11} \pm 1.33\bullet10^{-11}$ m^2 which is highlighted in red.

3.5. Visualization technique

The X-ray phase contrast imaging apparatus developed in [21] was used. This technique allows to obtain three different images: absorption, refraction and scattering. Although in Ref. [20], we proved the suitability of scattering images to visualize the flow progression for a conventional resin at typical processing conditions, some drawbacks were pointed out. In particular, fingering associated with capillary dominated flows was hindered by an inter-tow signal close to that of partially saturated tows. In the current work we propose to use the conventional absorption image together with contrasting agents added to the model fluid to enhance fluid/fabric contrast and thus elucidate flow front patterns with an increased resolution. The same acquisition methodology as in Ref. [20] was carried out. In summary, images were taken at an averaged time of 9.2 s per acquisition and in order to entirely image the impregnation (imaging area is approximatively 70 mm × 70 mm), six different positions of the moving platform were defined corresponding to five vertical stage movements of 25 mm. Then, depending on the fluid speed the number of acquisitions per position was adapted. The image size was 1334 × 1331 pixels and the resulting pixel size was about 50 μm × 50 μm. The comparison between the images resulting from the use of the contrasting agent or not is shown in the supplementary information A.

Table 1
Impregnation experiments.

Test #	u[mm/s]	U[mm/s]	T[°C]	η[Pa•s]	Ca(•10^{-4}) [-]
1	0.082	0.045	25.4	0.074	1.02
2	0.213	0.117	26.7	0.072	2.58
3	0.258	0.142	22.8	0.080	3.47
4	0.429	0.236	25.0	0.075	5.41

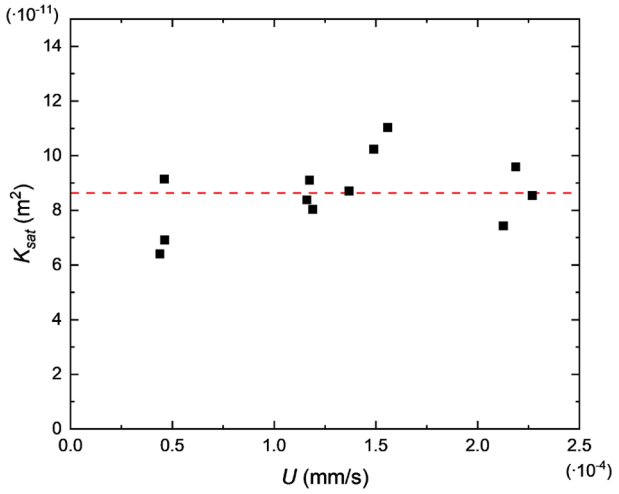

Fig. 3. Saturated permeability results.

3.6. Methodology to build the saturation curve

For each experiment, the saturation curve $S(z,t)$ was built as a function of location z in the fabric and impregnation time t. The same routine for flow front tracking and subsequent image analysis to build the saturation curve from the grayscale of X-ray images as in Ref. [20] was employed. A region of interest of 500 pixels was selected, corresponding to a width of 2.5 cm approximately located in the middle of the sample to get rid of flow edge effects. The averaged pixel intensity value over fabric width was calculated and converted into saturation value by comparing the pixel intensity values to those corresponding to fully wet and fully dry states. Saturation value extraction was calibrated to ensure that the value always remained between 0 (fully dry state) and 1 (final state after flushing the resin for several minutes, assuming complete saturation).

3.7. Numerical modeling

Infiltration experiments were all carried out with the same fluid and fibrous preform. A requirement for the developed model is to know in advance if the fluid progresses with a wetting or a non-wetting behavior. This was visually determined by observation of the dynamic flow front: if flow within the tows led the overall flow front, the fluid was considered as wetting for this range of flow rates, whereas if flow within the tows lagged, the fluid was considered as the non-wetting phase (and air

the wetting phase). As already introduced, Richards' differential equation is nonlinear and requires the definition of hydraulic properties as function of the saturation. Its solutions were numerically approximated thanks to a 1D model which was implemented to simulate the unidirectional flow in COMSOL Multiphysics 5.6; equations (9)-(13) were solved by the finite element method (FEM) with quadratic shape functions to find the resulting pressure field for the resin. Two models were thus developed to solve Eq. (9): one where the infiltrating resin is the wetting phase ($\alpha = w$, imbibition) and the other where it is the non-wetting phase ($\alpha = nw$, drainage). Since it is assumed that air pressure is zero, for the capillary leading case, the fluid pressure is defined by p_w thus $p_c = -p_w$. Analogously for the viscous leading case, the fluid pressure is p_{nw} and $p_c = p_{nw}$. The retention equations (10) and (12) define the fluid behavior in the capillary leading case and equations (11) and (13) the viscous leading case. To completely define the problem, initial and boundary conditions were set. At the inlet ($z = 0$ m), a normal inflow velocity equal to the superficial velocity U, representing the constant flow rate was set and at the outlet ($z = 0.15$ m), a no-flow condition (ensuring that no flow is entering at this point). Following a convergence study, the geometry was spatially discretized into a mesh with an element size of $5 \bullet 10^{-4}$ m resulting in 300 domain elements. An implicit backward differentiation formula method was used as stepping method for the time-dependent solver and a maximum time step of 0.1 s was set.

3.8. Parameters identification

As model parameters β, L and N are empirical parameters which cannot be directly measured, they were identified by solving an inverse problem. Building on the pythonic scripting interface for COMSOL, Mph (version 1.1.6) [48], a Python optimization procedure was implemented to fit the model over the experimental data. To perform the optimization, eleven $S(z,t)$ training curves were selected per experiment with the aim of representing various instances throughout the mold-filling. Then, the following four steps were carried out: (1) numerical results were extracted by evaluating the model at experimental times and saturation at experimental points was computed with a cubic spline interpolation; (2) the Weighted Mean Squared Error (WMSE) was calculated for each time and the error E for all curves was aggregated with the mean of the individual errors as:

$$E = \frac{1}{k}\sum_{i}^{k}\frac{\sum_{j}^{n} w_j \left(S(z_j,t_i)_{sim} - S(z_j,t_i)_{exp}\right)^2}{\sum_{j}^{n} w_j} \tag{16}$$

where k is the number of selected times, n the number of data points, w_j the user defined weight (equal to 1 for the linear part of the curve, between S = 0.1 and S = 0.9, and 10 for the rest), $S(z_j,t_i)_{sim}$ and $S(z_j,t_i)_{exp}$ are respectively modeled and experimental saturation data of the i^{th} time at j^{th} position. As the saturation curves are almost self-similar over the position z and linear over a large domain, the MSE resulted in the fitting of the average linear region. Thus, the WMSE was used to increase the weight of the non-linear region, namely below 0.1 and over 0.9 saturation by assigning the value of w_j accordingly. The error E was measured for more than 15,000 combinations of β, L and N over a large range of values (β = [1, 100], L = [-2, 0] and N = [1,30]) to build a surface response plot; (3) the combinations of parameters giving an error value up to 20 % of the lowest error were selected as initial inputs for the optimization routine. The equation (16) was set as objective function and minimized. However, it is crucial to notice that the saturation $S(z_j,t_i)_{sim}$ is the output of the FEM. Therefore, it is impossible to obtain the objective function derivatives directly with respect to the input parameters. Furthermore, the response is not linear and exhibits several local minima. The optimization was thus performed with one of the Nelder-Mead, Powell, Dual Annealing, or Differential Evolution algorithms implemented in Scipy (version 1) [49] to overcome these limitations. The Nelder-Mead algorithm based on a heuristic computation [50,51] was found to offer the best compromise between result quality and convergence speed and the Differential Evolution to better minimize the error at the expense of long convergence times; (4) the quality of the fitting was checked by computing the error E for additional validation curves that were not used in the optimization. Finally, the problem was constrained by setting upper and lower boundaries for the different parameters and the maximum number of iterations was set to 1000 [32,52].

4. Results

4.1. Flow experiments

An example of a sequence of three images per experiment taken at different times is shown in Fig. 4, for the four experiments. The fluid appears in black so the resulting flow regimes can be identified with this approach. Capillary fingering is clearly observed for test #1, with flow leading within the tows, resulting in an unsaturated length up to 20 mm. Moreover, inter-tow *meso*-voids resulting from strong capillary effects are apparent for this case as can be noticed in Fig. 4. Test #2 shows a slight capillary behavior and test #3 turned out to be a rather balanced flow with a small unsaturated zone. For both experiments, the unsaturated length was close to 10 mm. Viscous fingering is observed for test #4 with a larger unsaturated area (up to 15 mm), and flow leading between the tows. In this last case, the front is slightly more blurred due to the nesting induced changes in the *meso*-porosity network. Thus, for experiments #1 and #2, the resin is considered wetting and for #3 and #4 non-wetting. The fabric architecture and in particular the presence of the horizontal stitches were found to significantly affect the flow pattern. In the capillary-driven case, fiber bundles create "pools" in the upstream areas which lead to *meso*-void entrapment as shown in the sequence of images in Fig. 4 and explained in Fig. 5(a). In the viscous case, they form large empty areas within the fibrous preform leading to a stabilization of the flow as shown in Fig. 5(b). As a result, the saturation as a function of position results in an almost linear decrease over the unsaturated area for all cases. The pressure difference between the inlet and the outlet ΔP shows a linear behavior with time in all cases as expected, as illustrated in Fig. 6. Moreover, for tests #3 and #4, the pressure does not increase immediately because no pressure builds up at the inlet in the early phases of flow due to capillary wicking, which confirms our previous visual observations [1]. However, due to the low pressure values of the current experiments, these could not be exploited to directly evaluate a capillary pressure drop, as was done in Ref. [1].

4.2. Numerical simulation and optimization

The numerical simulations were carried out for the four injection conditions with the aim of exploiting $S(z,t)$ curves to extract $S(p_c)$ and $k_r(S)$. According to the previous observations, tests #1 and #2 were modelled as a wetting infiltrating fluid displacing non-wetting air and conversely, #3 and #4 as a non-wetting fluid displacing wetting air. Table 2 lists the times t_i used for the optimization of $S(z,t)$ curves. Those were selected so that the flow front was between 20 and 130 mm from the inlet with an increment of 10 mm approximately, giving a representative section of almost the entire steady fabric impregnation.

With the aim of determining the fitting parameters with accuracy, the error E between experimental and numerical data was calculated for several combinations of β, L, N and then the best candidates (giving smaller error) were used as inputs to the optimization routine. Details of the optimization procedure are provided in Supplementary information B. The minimized aggregated error E as well as the optimized β, L, N and resulting M values are presented in Table 3. A general trend was observed for β that increases as Ca decreases as Nordlund previously observed [11] and the inverse for N that increases with Ca, even though values of N for drainage experiments were very close. Finally, L was

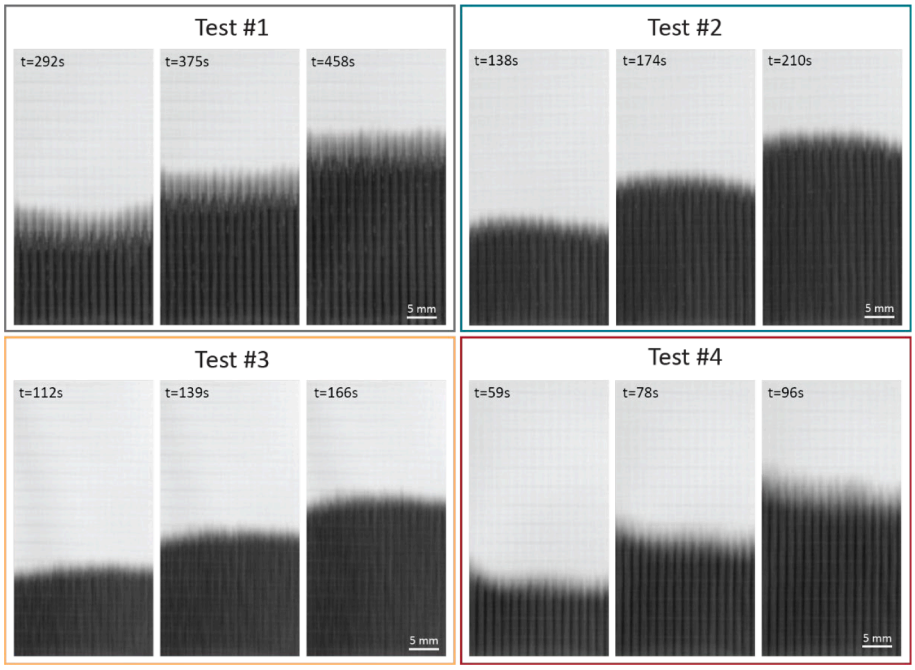

Fig. 4. X-ray absorption images showing the flow progression at three different times for the four injection conditions.

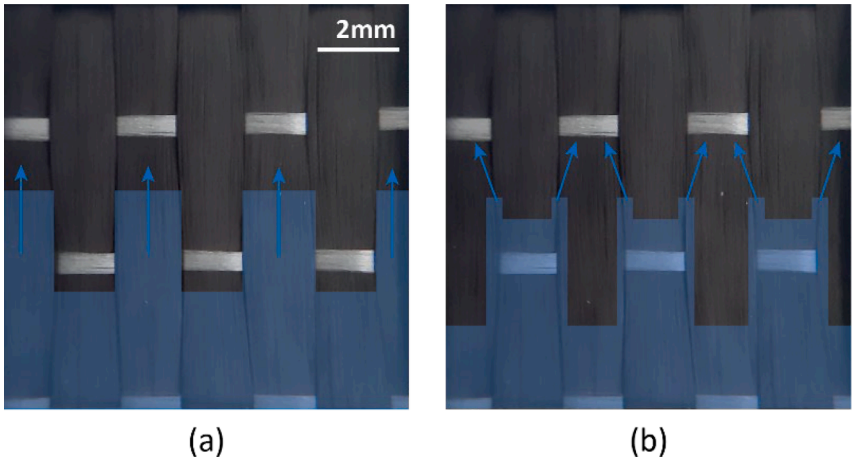

Fig. 5. Schematic of the influence of the fabric architecture on (a) capillary and (b) viscous flow patterns.

found negative in all cases similarly to Refs. [11,31,32].

The numerical simulations using the optimized parameters are compared with the experimental data in Fig. 7. For flow regimes close to a balance between capillary and viscous forces (tests #2 and #3), the saturation curves are very similar and the curve fitting matches almost perfectly. For viscous and capillary flows, since the flow front is slightly time-variant due to potential slight fiber rearrangements and more pronounced dual-scale effects, saturation curve shapes differ more along the fabric length and experimental times. For all cases, the saturation curves were quite steep due to a relatively small and rather stable unsaturated area as observed in Figs. 4 and 5, a characteristic dictated by the fabric geometry more specifically by the transverse stitches that limits extensive capillary flow before filling the larger gaps around themselves.

4.3. Hydraulic functions as a function of capillary regime

Previous results allowed to build the hydraulic functions describing the unsaturated flow behavior for the experimental injections. The relative permeability versus the liquid saturation functions $k_r(S)$ obtained by modelling the different flow regimes with the optimized parameters from Table 3 are given in Fig. 8. The shape of the curve differs when fluid is treated either as non-wetting (increasing concave) or wetting (increasing convex) even though this is more pronounced for capillary leading cases compared to viscous leading cases where curves present almost a linear profile as already suggested by Nordlund et al. [11]. Moreover, it is observed that the relative permeability is an increasing function of flow rate (and consequently of the *Ca*) for a given saturation level. Current results agree with published data since concave to convex shapes for wetting and non-wetting fluids as well as the displacement rate and wettability effects on the relative permeability have already largely been reported in literature for non-fibrous media [53–56]. This result can also be intuitively understood in our case, since we expect that fluid fills mostly the intra-tow region in the low *Ca* case, leading to a low value of relative permeability, whereas the fluid fills mostly the inter-tow regions in the high *Ca* case, leading to a higher value of relative permeability, since the large spaces between tows mostly govern the permeability.

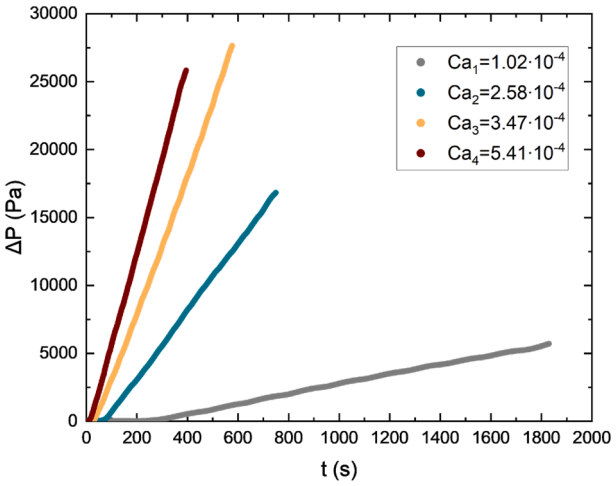

Fig. 6. ΔP inlet pressure measurements.

Table 2
Selected instances for optimization.

Times (s)	Test #1	Test #2	Test #3	Test #4
t_1	236.9	91.5	76.1	49.3
t_2	347.1	138.1	121.3	68.1
t_3	467.1	183.4	156.9	96.4
t_4	577.0	228.8	195.5	116.0
t_5	697.9	275.9	231.9	143.4
t_6	825.5	330.6	278.0	161.8
t_7	960.2	377.9	313.9	180.8
t_8	1087.0	422.6	349.6	207.4
t_9	1204.4	468.1	395.0	234.6
t_{10}	1332.4	514.1	431.4	252.8
t_{11}	1442.8	560.3	466.7	280.0

Table 3
Parameters identification results.

Test #	Model	β[m^{-1}]	L[-]	N[-]	M[-]	$E(10^{-3})$ [-]
1	Wetting	26.79	−1.09	3.00	0.67	2.362
2	Wetting	14.39	−1.07	5.04	0.80	0.202
3	Non-wetting	4.70	−0.78	19.41	0.95	0.217
4	Non-wetting	2.43	−0.90	20.85	0.95	0.780

Similarly, the respective retention functions $S(p_c)$ were obtained and are presented in Fig. 9. It should be noted that ΔP_γ boundaries shown on the figure will be discussed thereafter on section 4.4. Drainage curves (describing tests #3 and #4) were found to be rate dependent: for the fastest flow rate (test #4), the unsaturated region is spread over of a wider range of capillary pressures when compared to the lower flow rate (test #3). Thus, increasing the flow rate results in a less steep drainage curve, indicating a larger unsaturated zone with a large distribution of capillary pressures. The drainage curve dependency on the flow rate to describe unsaturated flow in dual-scale fabrics was already observed by Nordlund et al. [11] and related to the dynamic wetting conditions. However, the same trend was not observed in imbibition curves (describing tests #1 and #2) which were very similar for both injection cases even though the pressure at smaller saturation rates was found to be higher for the slower case (test #1) as suction in the tows is higher. The imbibition curve of test #1 is in fact very close to spontaneous imbibition in static conditions (which corresponds to a wicking experiment), since the pressure increase is very low, as shown in Fig. 4. Conversely, in drainage, narrow pores between bundles affect the $S(p_c)$ curve and the entrance pressure effect shifts the curve to higher positive values. This was also observed by Smiles et al. [57], who found retention curves to be non-unique during drainage (dynamic drainage curves present higher suction than static ones) whereas dynamics effects are not observable during imbibition and the retention description is unique. In other words, since the dynamic effects depend on the pressure change, the retention curve is also influenced by the pressure head caused by viscous effects, which is more important at high flow rates [58].

Finally, it is of interest to point out that the attribution of the liquid phase to a wetting or a non-wetting phase was made here based on our observation of the flow front. As a result, tests #2 and #3 show very similar saturation curves $S(z,t)$ because they are close to the balanced regime but the $k_r(S)$ and $S(p_c)$ descriptions are very different, since one is considered an imbibition whereas the other one was considered as a drainage experiment. For intermediate flows, capillary and viscous fingering are hardly discernable in the unsaturated length and in addition, the unsaturated length is even more sensitive to the flow front shape when compared to viscous or capillary dominated flows. Thus, it is tricky for intermediate flows to define sharp boundaries between the two wetting conditions since there is not a given speed at which a fluid pass from wetting to non-wetting behavior but rather an interval of speeds at which both coexist, regarded in literature as crossover pattern [59]. This is why the multiphase approach can be limiting when considering the capillary to viscous leading flows transition state.

The determination of $p_c - S - k_r$ relationships, defined in this work by equations (10)-(13), is essential to model unsaturated flows with a two-phase flow approach. These parameters are affected by fluid and porous media properties but how is still a subject of intense research [56]. Commonly, they are fitted to experimental data based on stationary measurements and the non-uniqueness of these relationships, in particular in dynamic conditions, is well acknowledged in soil science literature for both drainage and imbibition phenomena [60]. In particular, the dynamic effect was shown to be more significant for low permeability porous media [61] and was proven to be impacted by several factors such as porous medium and fluid properties as well as some external factors [39]. In soil science, the averaged pore throat size has been shown to have the greatest impact leading to a constant redistribution of fluid flow at the pore scale. In our case, where liquid resins flow through fibrous porous media, with rather stable pore sizes over the length of the preform, the wettability proved to be a dynamic property highly influencing the relative movement and distribution of fluid inside the porous medium at the macro-scale and thus the flow descriptions p_c and k_r [1,5,62]. Current results show that dynamic wettability results in a change of the hydraulic descriptions. Concerning the relative permeability curve, a decrease of Ca corresponding to an increasingly capillary dominated flow pattern led to a decrease of the relative permeability for a given saturation value. Since the relative permeability reflects the connected pathway of flow based on saturation distribution, it seems logical that viscous flow dominated cases present high k_r values at the Darcy scale when compared to capillary dominated flows (permeability values far from K_{sat}). For the drainage cases, the relative permeability function is almost linear; this can be attributed to the dominant flow taking place in *meso*-spaces, so that the overall permeability is expected to be close to the saturated permeability, as was already noted in previous work [44,63,64]. It should be noted that some authors questioned the use of the saturated permeability K_{sat} for the definition of the Darcy's permeability since the K_{sat} is sensitive to the flow in *meso*-pores and unsaturated flows occur across all the pore scale range [32].

Although capillary pressure plays a major role in the description of fluid flow in unsaturated porous media, the theoretical basis and practical implications of it remain poorly understood [35]. In static conditions, there is only one capillary pressure p_c which depends on the system and is described as the pressure difference between the wetting and non-wetting phases as described earlier. However, in dynamic conditions, p_c also depends on the saturation speed $\dot{S}$ and the difference between pressures is not only due to capillary effects close to

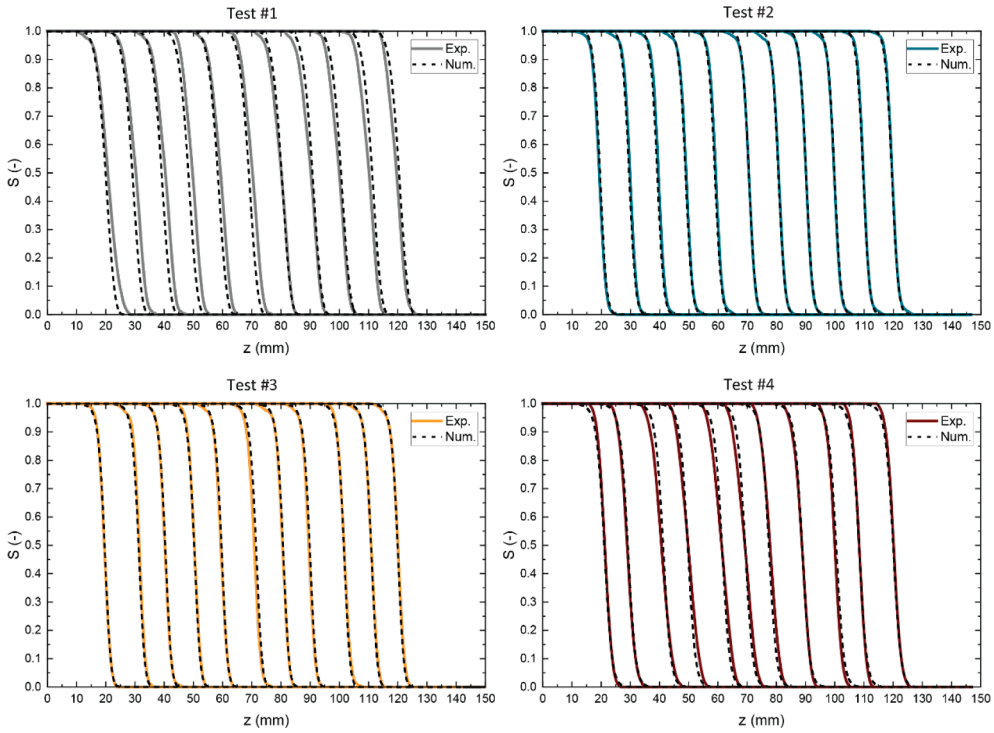

Fig. 7. Experimental and numerical $S(z, t_i)$ curves.

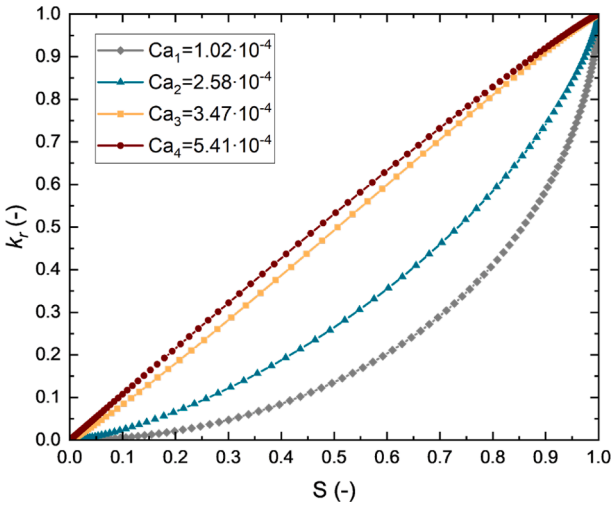

Fig. 8. Hydraulic relative permeability function.$k_r(S)$.

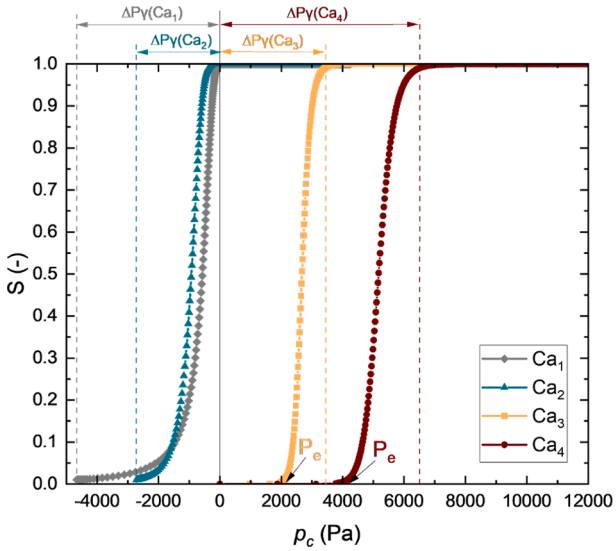

Fig. 9. Hydraulic retention function.$S(p_c)$.

equilibrium but also to the pressure gradient needed to overcome the viscous forces. In the present work, we show that wettability also influences the $S(p_c)$ relationship. In drainage processes, we observed that a higher flow rate results in a decrease of the system wettability and thus a higher capillary pressure is observed for a given saturation. Conversely, in imbibition processes, a higher wettability has a small impact on the capillary pressure description [35,36,60,65,66]. Dynamic forces are highly scale dependent and although several studies agreed on the influence of the dynamic effects in drainage processes, a consensus on how dynamic effects affect imbibition processes at large scales has not been reached so far given the interplay of physical phenomena happening at the microscale [67–69].

4.4. Comparison with the slug-flow approach

In fully saturated flow studies, following a slug-flow approach, capillary effects are lumped into a capillary pressure drop at the flow front ΔP_γ, defined as the pressure difference between the local pressure in the fully saturated fluid phase just behind the infiltration front and the pressure in the preform ahead of the infiltration front [24,70]. With this approach, Verrey et al. [1] showed the velocity dependence of the capillary pressure drop and the dynamic contact angle using the Hoffman-Voinov-Tanner law [2,71]:

$$\Delta P_\gamma = -S_f \gamma \cos\left(\sqrt[3]{c_T Ca + \theta_0^3}\right) \tag{17}$$

where S_f is the liquid-fiber interface per unit volume of liquid, c_T the empirical Tanner coefficient and θ_0 the static contact angle. With the aim of evaluating the difference between a capillary pressure drop evaluated using the slug flow approach, and our approach, and aiming to characterize the relationship between capillary effects and wetting changes, the capillary pressure drop ΔP_γ was estimated in our four experiments. Since we could not make use of the pressure curves (as performed in Ref. [1]), due to the relatively low precision of the injection pump impacting the pressure readings at very low pressure regime, we evaluated the pressure difference between the beginning and end of the unsaturated region from the simulation results as $\Delta P_\gamma = p(S = 0.99) - p(S = 0.01)$, with p the pressure in the fluid phase, as illustrated in Fig. 10 for test#1 case at time t_4. The values are then correlated to the capillary pressure curves found using the multiscale flow approach as reported in Fig. 9. The capillary pressure drop ΔP_γ indeed corresponds to the distance between $p_c = 0$ and $p_c(S = 0.01)$ for imbibition and $p_c(S = 0.99)$ for drainage. It can be remarked that for imbibition curves, the overall ΔP_γ is equal to the capillary pressure curve since the flow in the unsaturated region progresses only due to capillary effects whereas for the drainage case, ΔP_γ corresponds to a pressure P_e (or entry pressure) that should be overcome so the non-wetting liquid starts displacing the wetting fluid plus the capillary pressure needed to fill all the pores as previously suggested. This approach can be directly related to the relative position of the flow fronts within the tows and in the *meso*-space region: indeed, this approach means that locally, the local pressure in the tows is lower, or higher as compared to the local pressure between the tows, which must be closer to atmospheric pressure, since the wetted perimeter is small as compared to the air-fluid surface in these areas. Thus, the resulting average pressure close to the flow front is negative or positive and is related to the dynamic capillary pressure identified in this work. We explore the idea to compare this to a dynamic contact angle to find out if it is possible to make the link between the multiphase flow approach and the usual slug-flow approach often used in composite processing. We nonetheless keep in mind that a more detailed, local scale analysis would be required to explore the limits of this approach, in particular when the separation of scales between inter- and intra-tow regions becomes large.

Thus, S_f was calculated assuming fibers as perfect cylinders of radius r_f as:

$$S_f = \frac{2}{r_f}\left(\frac{V_f}{1 - V_f}\right) \tag{18}$$

leading to an estimated value of $S_f = 467{,}532\ \mathrm{m}^{-1}$. However, as suggested in Ref. [1], the use of equation (17) is very sensitive to the value of S_f and a more accurate measurement could be necessary. Fig. 11 shows a representative drop of fluid onto a carbon fiber extracted from the fabric. The static contact angle value of $23.4° \pm 4.6°$ was obtained by averaging the measurements for 50 drops. Analogously to Verrey's work, the experimental values of capillary pressure drop were plotted against the capillary number to illustrate the influence of the fluid velocity on capillary effects and fitted to equation (17), and c_T was found to be equal to 14,510 (Fig. 12(a)). The evolution of the capillary pressure drop is directly linked to the dynamic contact angle θ which can be easily determined by Tanner's law (Fig. 12(b)):

$$\theta^3 - \theta_0^3 \cong c_T Ca \tag{19}$$

Despite the differences in original assumptions between slug-flow and two-phase flow approaches, the results revealed to align well when converged with the definition of the dynamic contact angle, which can be considered here as an averaged contact angle, since it is extracted from a volume averaged measurement.

Current capillary pressure values (and the location of the optimal capillary number, when the dynamic contact angle is 90°) were found to be rather low when compared to literature [1,11]; this was attributed to the volume fraction which was less than 50 % in our case and the strong wettability of our liquid (with low surface tension and contact angle). This methodology is however not restricted to the use of model fluids, in particular when using X-ray phase contrast which does not require the addition of contrasting agents, and further tests can be carried out following this methodology with epoxy resins and higher volume fractions.

5. Conclusions

A methodology was presented to analyze the progressive saturation of a carbon fabric preform. Impregnation under constant flow rate was visualized by means of conventional X-ray radiography. Taking advantage of an enhanced absorption contrast between the low-density fibers and the high intensity signal of a model fluid containing contrasting agents, the corresponding dynamic saturation curves were built. Then, a two-phase flow model inspired from soil-science was applied to numerically describe the infiltration of the fluid into the dry preform for wetting and non-wetting systems. Hydraulic functions $S(p_c)$ and $k_r(S)$ were obtained by fitting experimental and numerical $S(z,t)$ curves and finding Van Genuchten and Mualem's parameters with a heuristic

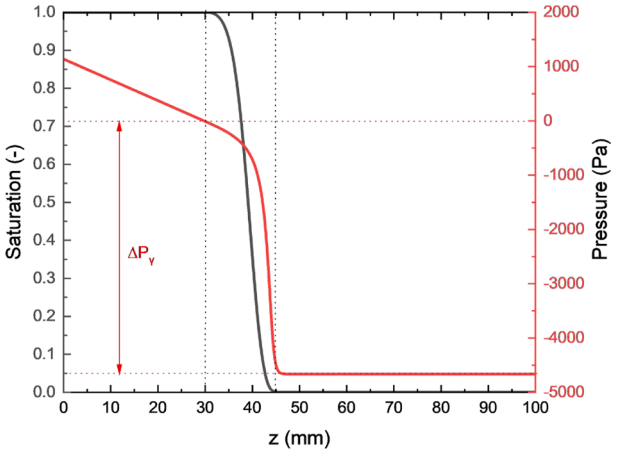

Fig. 10. Schematic representation of ΔP_γ determination from the saturation (in black) and pressure (in red) of the fluid phase versus the position z. Example from test #1.

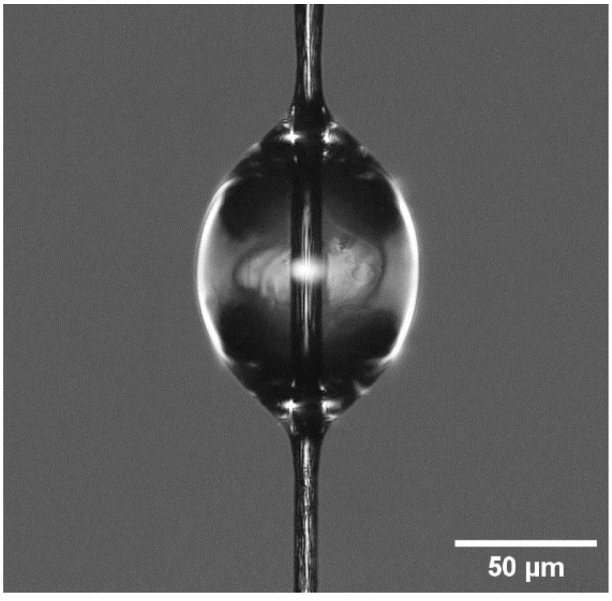

Fig. 11. Drop analysis on a carbon fiber.

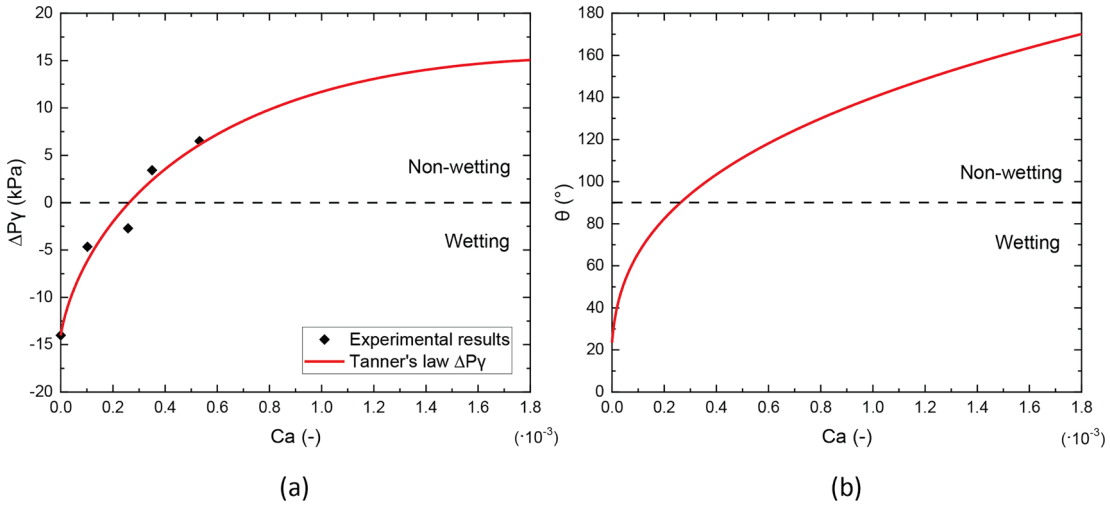

Fig. 12. (a) Influence of the fluid velocity on the capillary pressure drop and (b) resulting $\theta(Ca)$ curve.

optimization algorithm. The effect of the capillary number on hydraulic functions was elucidated and found to be in accordance with the literature from soil science. In the current work, simple 1D models have been developed but can be easily extrapolated to 2D or 3D simulations in COMSOL or other numerical codes, to represent impregnation of parts with more complex geometries. Moreover, a simple correlation was found between the multiscale flow approach and the slug-flow assumption allowing to build the dynamic contact angle and capillary pressure versus the capillary number from the progressive saturation analysis. Those results emphasize the validity and usefulness of the slug-flow assumption employed in previous works [1,44,70] and give new insights on the multiphase flow method.

Two-phase flow models are used in many engineering branches leading to a very well-documented topic but unfortunately barely developed in the frame of LCM infiltration where the *meso* and micro-structure exhibits rather anisotropic features unlike other domains. Moreover, some observed natural phenomena such as the effect of swelling media [72–75] or the significant air entrapment mechanism happening during imbibition (since the pore scale invasion mechanisms are more complex) when compared to drainage [76,77], can be extrapolated to impregnation studies that would encourage the use of this approach. For that purpose, this work has gone some way towards promoting the application of two-phase models in the frame of LCM infiltration. In case of textiles with larger *meso*-channels, leading to a very clear dual-scale morphology, the use of a superposition of saturation curves could be investigated, as proposed in fractured porous media, and a more local approach, considering flow in inter- and intra-tow regions separately would be of interest. In addition, since hydraulic functions are directly linked to flow kinetics happening at the pore-scale, it is sought in further work, to investigate the effects of wettability and porous medium configuration on the flow invasion patterns and consequently on these continuous descriptions at the macro-scale, with a deep insight on intermediate states at which a fluid potentially switches from a wetting to a non-wetting state.

CRediT authorship contribution statement

Helena Teixidó: Investigation, Methodology, Software, Validation, Writing – original draft. **Guillaume Broggi:** Methodology, Software, Writing – review & editing. **Baris Caglar:** Methodology, Supervision, Formal analysis, Writing – review & editing. **Véronique Michaud:** Conceptualization, Funding acquisition, Project administration, Supervision, Writing – review & editing.

Declaration of Competing Interest

The authors declare that they have no known competing financial interests or personal relationships that could have appeared to influence the work reported in this paper.

Data availability

Data will be made available on request.

Acknowledgements

This work was supported by the Swiss National Science Foundation (SNF n° 200021_182669). The authors acknowledge Jeroen Staal for his contribution in the parameters' identification procedure development and Valentin Rougier for his constructive comments. The authors also thank the SMaL laboratory at EPFL for use of their Drop Shape Analyzer.

Appendix A. Supplementary material

Supplementary data to this article can be found online at https://doi.org/10.1016/j.compositesa.2023.107520.

References

[1] Verrey J, Michaud V, Manson JA. Dynamic capillary effects in liquid composite moulding with non-crimp fabrics. Compos Part A Appl Sci Manuf 2006;37:92–102. https://doi.org/10.1016/j.compositesa.2005.04.011.
[2] Kistler SF. Hydrodynamics of wetting. In: Berg JC, editor. Wettability. 1st ed., Marcel Dekker Inc., New York; 1993, p. 311–429.
[3] Leclerc JS, Ruiz E. Porosity reduction using optimized flow velocity in Resin Transfer Molding. Compos A 2008;39:1859–68. https://doi.org/10.1016/j.compositesa.2008.09.008.
[4] Teixidó H, Staal J, Caglar B, Michaud V. Capillary Effects in Fiber reinforced polymer composite processing: a review. Front Mater 2022;9:1–24. https://doi.org/10.3389/fmats.2022.809226.
[5] Michaud V. A review of non-saturated resin flow in liquid composite moulding processes. Transp Porous Media 2016. https://doi.org/10.1007/s11242-016-0629-7.
[6] Bear J. Modeling phenomena of flow and transport in porous media. Springer; 2018.
[7] Léger A, Weber L, Mortensen A. Influence of the wetting angle on capillary forces in pressure infiltration. Acta Mater 2015;91:57–69. https://doi.org/10.1016/j.actamat.2015.03.002.
[8] Léger A, Molina-Jordá JM, Weber L, Mortensen A. Percolation and universal scaling in composite infiltration processing. Mater Res Lett 2015;3:7–15. https://doi.org/10.1080/21663831.2014.948692.
[9] Schneider G, Weber L, Mortensen A. Reactive pressure infiltration of Cu-46at.pct. Si into carbon. Acta Mater 2019;177:9–19. https://doi.org/10.1016/j.actamat.2019.07.010.

[10] Varnavides G, Mortensen A, Carter WC. Simulating Infiltration as a Sequence of Pinning and De-pinning Processes. Acta Mater 2021:210. https://doi.org/10.1016/j.actamat.2021.116831.

[11] Nordlund M, Michaud V. Dynamic saturation curve measurement for resin flow in glass fibre reinforcement. Compos A 2012;43:333–43. https://doi.org/10.1016/j.compositesa.2011.12.001.

[12] Villière M, Guéroult S, Sobotka V, Boyard N, Bréard J. Dynamic saturation curve measurement in liquid composite molding by heat transfer analysis. Compos A 2015;69:255–65. https://doi.org/10.1016/j.compositesa.2014.11.024.

[13] Gascón L, García JA, Lebel F, Ruiz E, Trochu F. Numerical prediction of saturation in dual scale fibrous reinforcements during Liquid Composite Molding. Compos A 2015;77:275–84. https://doi.org/10.1016/j.compositesa.2015.05.019.

[14] Gascón L, García JA, Lebel F, Ruiz E, Trochu F. A two-phase flow model to simulate mold filling and saturation in Resin Transfer Molding. Int J Mater Form 2016;9:229–39. https://doi.org/10.1007/s12289-015-1225-z.

[15] Brooks RH, Corey AT. Hydraulic Properties of Porous Media. Fort Collins: Colorado State University Hydrology Papers; 1964.

[16] van Genuchten MT. A closed-form equation for predicting the hydraulic conductivity of unsaturated soils. Soil Science Society American Journal 1980;44:892–8. https://doi.org/10.1016/j.pan.2017.07.214.

[17] Carlone P, Palazzo GS. Unsaturated and saturated flow front tracking in liquid composite molding processes using dielectric sensors. Appl Compos Mater 2015;22:543–57. https://doi.org/10.1007/s10443-014-9422-3.

[18] Carlone P, Rubino F, Paradiso V, Tucci F. Multi-scale modeling and online monitoring of resin flow through dual-scale textiles in liquid composite molding processes. Int J Adv Manuf Technol 2018;96:2215–30. https://doi.org/10.1007/s00170-018-1703-9.

[19] Castro J, Sket F, Helfen L. In situ local imaging and analysis of impregnation during liquid moulding of composite materials using synchrotron radiation computed laminography. Compos Sci Technol 2021:215. https://doi.org/10.1016/j.compscitech.2021.108999.

[20] Teixidó H, Caglar B, Revol V, Michaud V. In-operando dynamic visualization of flow through porous preforms based on X-ray phase contrast imaging. Compos Part A Appl Sci Manuf 2021:149. https://doi.org/10.1016/j.compositesa.2021.106560.

[21] Gresil M, Revol V, Kitsianos K, Kanderakis G. EVITA Project : comparison between traditional non-destructive techniques and phase contrast X-Ray imaging applied to aerospace carbon fibre reinforced polymer. Appl Compos Mater 2017;24:513–24. https://doi.org/10.1007/s10443-016-9540-1.

[22] Gerke HH, van Genuchten MT. A dual porosity model for simulating the preferential movement of water and solutes in structured porous media. Water Resour Res 1993;29:305–19. https://doi.org/10.1029/92WR02339.

[23] Coppola A. Unimodal and bimodal descriptions of hydraulic properties for aggregated soils. Soil Sci Soc Am J 2000;64:1252–62. https://doi.org/10.2136/sssaj2000.6441252x.

[24] Michaud V, Mortensen A. Infiltration processing of fibre reinforced composites: governing phenomena. Compos Part A Appl Sci Manuf 2001;32:981–96. https://doi.org/10.1016/S1359-835X(01)00015-X.

[25] Darcy H. Les fontaines publiques de la ville de Dijon. Paris: Dalmont, Victor; 1856.

[26] Freeze RA. Three-dimensional, Transient, Saturated-unsaturated Flow in a Groundwater Basin. Water Resour Res 1971;7.

[27] Mualem Y. Hydraulic conductivity of unsaturated porous media- generalized macroscopic approach. Water Resour Res 1978;14:325–34.

[28] Mualem Y. A new model for predicting the hydraulic conductivity of unsaturated porous media. Water Resour Res 1976;12:513–22.

[29] Kosugi K. Lognormal distribution model for unsaturated soil hydraulic properties. Water Resour Res 1996;32:2697–703. https://doi.org/10.1029/96WR01776.

[30] Bjørnarå TI, Aker E. Comparing Equations for Two-Phase Fluid Flow in Porous Media. COMSOL Conference, Hannover: 2008.

[31] Peters A, Durner W, Wessolek G. Consistent parameter constraints for soil hydraulic functions. Adv Water Resour 2011;34:1352–65. https://doi.org/10.1016/j.advwatres.2011.07.006.

[32] Schaap MG, Leij FJ. Improved Prediction of Unsaturated Hydraulic Conductivity with the Mualem-van Genuchten Model. Soil Sci Soc Am 2000;64:843–51. https://doi.org/10.2136/sssaj2000.643843x.

[33] Løvoll G, Jankov M, Måløy KJ, Toussaint R, Schmittbuhl J, Schäfer G, et al. Influence of viscous fingering on dynamic saturation-pressure curves in porous media. Transp Porous Media 2011;86:305–24. https://doi.org/10.1007/s11242-010-9622-8.

[34] Schultze B, Ippisch O, Huwe B, Durner W. Dynamic Nonequilibrium During Unsaturated Water Flow. Proceedings of the International Workshop on Characterization and Measurement of the Hydraulic Properties of Unsaturated Porous Media, Riverside, CA: 1999.

[35] Hassanizadeh SM, Celia MA, Dahle HK. Dynamic effect in the capillary pressure-saturation relationship and its impacts on unsaturated flow. Vadose Zone J 2002;1:38–57. https://doi.org/10.2136/vzj2002.3800.

[36] Zhuang L, Duijn CJ, Hassanizadeh SM. The effect of dynamic capillarity in modeling saturation overshoot during infiltration. Vadose Zone J 2019;18:1–14. https://doi.org/10.2136/vzj2018.07.0133.

[37] Bottero S, Hassanizadeh SM, Kleingeld PJ, Heimovaara TJ. Nonequilibrium capillarity effects in two-phase flow through porous media at different scales. Water Resour Res 2011:47. https://doi.org/10.1029/2011WR010887.

[38] Manthey S, Hassanizadeh SM, Helmig R. Macro-scale dynamic effects in homogeneous and heterogeneous porous media. Transp Porous Media 2005;58:121–45. https://doi.org/10.1007/s11242-004-5472-6.

[39] Chen Y, Mao Y, Yang L, Wei W, Meng Q, Cai J. A Comprehensive review of factors affecting dynamic capillary effect in two-phase flow. Transp Porous Media 2022. https://doi.org/10.1007/s11242-021-01723-x.

[40] Li Y, Liu C, Li H, Chen S, Lu K, Zhang Q, et al. A review on measurement of the dynamic effect in capillary pressure. J Pet Sci Eng 2022:208. https://doi.org/10.1016/j.petrol.2021.109672.

[41] Cai JC, Chen Y, Qiao JC, Yang L, Zeng JH, Sun CH. Determination of dynamic capillary effect on two-phase flow in porous media: a perspective from various methods. Pet Sci 2022. https://doi.org/10.1016/j.petsci.2022.01.017.

[42] Kassa AM, Gasda SE, Kumar K, Radu FA. Impact of time-dependent wettability alteration on the dynamics of capillary pressure. Adv Water Resour 2020:142. https://doi.org/10.1016/j.advwatres.2020.103631.

[43] Friedman SP. Dynamic contact angle explanation of flow rate-dependent saturation-pressure relationships during transient liquid flow in unsaturated porous media. J Adhes Sci Technol 1999;13:1495–518. https://doi.org/10.1163/156856199X00613.

[44] Salvatori D, Caglar B, Teixidó H, Michaud V. Permeability and capillary effects in a channel-wise non-crimp fabric. Compos A 2018;108:41–52. https://doi.org/10.1016/j.compositesa.2018.02.015.

[45] Sket F, Enfedaque A, Alton C, González C, Molina-Aldareguia JM, Llorca J. Automatic quantification of matrix cracking and fiber rotation by X-ray computed tomography in shear-deformed carbon fiber-reinforced laminates. Compos Sci Technol 2014;90:129–38. https://doi.org/10.1016/j.compscitech.2013.10.022.

[46] Engineering ToolBox. Surface Tension 2005. https://www.engineeringtoolbox.com/surface-tension-d_962.html (accessed January 16, 2023).

[47] Carroll BJ. The accurate measurement of contact angle, phase contact areas, drop volume, and laplace excess pressure in drop-on-fiber systems. J Colloid Interface Sci 1976;57:488–95.

[48] Hennig J, Elfner M, Feder J. MPh-py/MPh: MPh 1.1.6 2022.

[49] Virtanen P, Gommers R, Oliphant TE, Haberland M, Reddy T, Cournapeau D, et al. SciPy 1.0: fundamental algorithms for scientific computing in Python. Nat Methods 2020;17:261–72. https://doi.org/10.1038/s41592-019-0686-2.

[50] Gao F, Han L. Implementing the Nelder-Mead simplex algorithm with adaptive parameters. Comput Optim Appl 2012;51:259–77. https://doi.org/10.1007/s10589-010-9329-3.

[51] Nelder JA, Meadf R. A simplex method for function minimization. Comput J 1965;7:308–13.

[52] Ippisch O, Vogel HJ, Bastian P. Validity limits for the van Genuchten-Mualem model and implications for parameter estimation and numerical simulation. Adv Water Resour 2006;29:1780–9. https://doi.org/10.1016/j.advwatres.2005.12.011.

[53] Tsakiroglou CD, Theodoropoulou MA, Karoutsos V. Nonequilibrium capillary pressure and relative permeability curves of porous media. AIChE J 2003;49:2472–86. https://doi.org/10.1002/aic.690491004.

[54] Tsakiroglou CD, Avraam DG, Payatakes AC. Transient and steady-state relative permeabilities from two-phase flow experiments in planar pore networks. Adv Water Resour 2007;30:1981–92. https://doi.org/10.1016/j.advwatres.2007.04.002.

[55] Nguyen VH, Sheppard AP, Knackstedt MA, Val PW. The effect of displacement rate on imbibition relative permeability and residual saturation. J Pet Sci Eng 2006;52:54–70. https://doi.org/10.1016/j.petrol.2006.03.020.

[56] Kassa AM, Gasda SE, Kumar K, Radu FA. Modeling of relative permeabilities including dynamic wettability transition zones. J Pet Sci Eng 2021:203. https://doi.org/10.1016/j.petrol.2021.108556.

[57] Smiles D, Vachaud G, Vauclin M. A test of the uniqueness of the soil moisture characteristic during transient, nonhysteretic flow of water in a rigid soil. Soil Sci Soc Am J 1971;35:534–9. https://doi.org/10.2136/sssaj1971.03615995003500040018x.

[58] Konangi S, Palakurthi NK, Karadimitriou NK, Comer K, Ghia U. Comparison of pore-scale capillary pressure to macroscale capillary pressure using direct numerical simulations of drainage under dynamic and quasi-static conditions. Adv Water Resour 2021:147. https://doi.org/10.1016/j.advwatres.2020.103792.

[59] Guo X, Liu R, Wang J, Shuai S, Xiong D, Bai S, et al. 3D actual microstructure-based modeling of non-isothermal infiltration behavior and void formation in liquid composite molding. Appl Math Model 2021;94:388–402. https://doi.org/10.1016/j.apm.2021.01.018.

[60] Hassanizadeh S. Upscaling multiphase flow in porous media. From pore to core beyond. Dordrecht: Springer; 2005.

[61] Zhang H, He S, Jiao C, Luan G, Mo S, Lei G. Investigation of dynamic effect of capillary pressure in ultra-low permeability sandstones. Indian Geotechn J 2015;45:79–88. https://doi.org/10.1007/s40098-014-0109-3.

[62] Nhunduru RAE, Jahanbakhsh A, Shahrokhi O, Wlodarczyk KL, Garcia S, Maroto-Valer MM. The impact of wettability on dynamic fluid connectivity and flow transport kinetics in porous media. Water Resour Res 2022:58. https://doi.org/10.1029/2021wr030729.

[63] Geoffre A, Ghestin M, Moulin N, Bruchon J, Drapier S. Bounding transverse permeability of fibrous media: a statistical study from random representative volume elements with consideration of fluid slip. Int J Multiph Flow 2021:143. https://doi.org/10.1016/j.ijmultiphaseflow.2021.103751.

[64] Geoffre A, Wielhorski Y, Moulin N, Bruchon J, Drapier S, Liotier PJ. Influence of intra-yarn flows on whole 3D woven fabric numerical permeability: from Stokes to Stokes-Darcy simulations. Int J Multiph Flow 2020:129. https://doi.org/10.1016/j.ijmultiphaseflow.2020.103349.

[65] Zhuang L, Hassanizadeh SM, Qin CZ, de Waal A. Experimental investigation of hysteretic dynamic capillarity effect in unsaturated flow. Water Resour Res 2017;53:9078–88. https://doi.org/10.1002/2017WR020895.

[66] Abbasi J, Ghaedi M, Riazi M. A multiscale study on the effects of dynamic capillary pressure in two-phase flow in porous media. Korean J Chem Eng 2020;37:2124–35. https://doi.org/10.1007/s11814-020-0645-8.
[67] Abbasi J, Ghaedi M, Riazi M. A new numerical approach for investigation of the effects of dynamic capillary pressure in imbibition process. J Pet Sci Eng 2018;162:44–54. https://doi.org/10.1016/j.petrol.2017.12.035.
[68] Zahasky C, Benson SM. Spatial and temporal quantification of spontaneous imbibition. Geophys Res Lett 2019;46:11972–82. https://doi.org/10.1029/2019GL084532.
[69] Harimi B, Masihi M, Mirzaei-Paiaman A, Hamidpour E. Experimental study of dynamic imbibition during water flooding of naturally fractured reservoirs. J Pet Sci Eng 2019;174:1–13. https://doi.org/10.1016/j.petrol.2018.11.008.
[70] Caglar B, Tekin C, Karasu F, Michaud V. Assessment of capillary phenomena in liquid composite molding. Compos A 2019;120:73–83. https://doi.org/10.1016/j.compositesa.2019.02.018.
[71] Mortensen A, Cornie JA. On the infiltration of metal matrix composites. Metall Trans A 1987;18:1160–3. https://doi.org/10.1007/BF02668570.
[72] Sweijen T, Nikooee E, Hassanizadeh SM, Chareyre B. The effects of swelling and porosity change on capillarity: DEM coupled with a pore-unit assembly method. Transp Porous Media 2016;113:207–26. https://doi.org/10.1007/s11242-016-0689-8.
[73] Chen T, Du M, Yao Q. Evolution of hydraulic conductivity of unsaturated compacted Na-bentonite under confined condition—including the microstructure effects. Materials 2022:15. https://doi.org/10.3390/ma15010219.
[74] Sweijen T, Hassanizadeh SM, Aslannejad H, Leszczynski S. The effect of particle shape on porosity of swelling granular materials: discrete element method and the multi-sphere approximation. Powder Technol 2020;360:1295–304. https://doi.org/10.1016/j.powtec.2019.09.036.
[75] Sweijen T, Hassanizadeh SM, Chareyre B. Unsaturated flow in a packing of swelling particles; a grain-scale model. Adv Water Resour 2020:142. https://doi.org/10.1016/j.advwatres.2020.103642.
[76] Wang Z, Feyen J, Nielsen DR, van Genuchten MT. Two-phase flow infiltration equations accounting for air entrapment effects. Water Resour Res 1997;33:2759–67. https://doi.org/10.1029/97WR01708.
[77] Wang Z, Feyen J, van Genuchten MT, Nielsen DR. Air entrapment effects on infiltration rate and flow instability. Water Resour Res 1998;34:213–22. https://doi.org/10.1029/97WR02804.